Electronic Supplementary Material (ESI) for Journal of Materials Chemistry A.
This journal is © The Royal Society of Chemistry 2020

Layer Conductance Reduction and Failure Analysis due to Bending for Superflexible Perovskite Solar Cell

Electronic Supplementary Information (ESI)

Ziang Xie[1], *Wanjin Xu*[1], *Shuren Sun*[1], *Xixi Xie*[1], *Yanping Li*[1] *and G. G. Qin*[1,2,*]

1: State Key Lab for Mesoscopic Physics, School of Physics, Peking University, Beijing 100871, People's Republic of China

2: Collaborative Innovation Center of Extreme Optics, Shanxi University, Taiyuan, Shanxi 030006, People's Republic of China

E-mail: qingg@pku.edu.cn

Supplementary figures

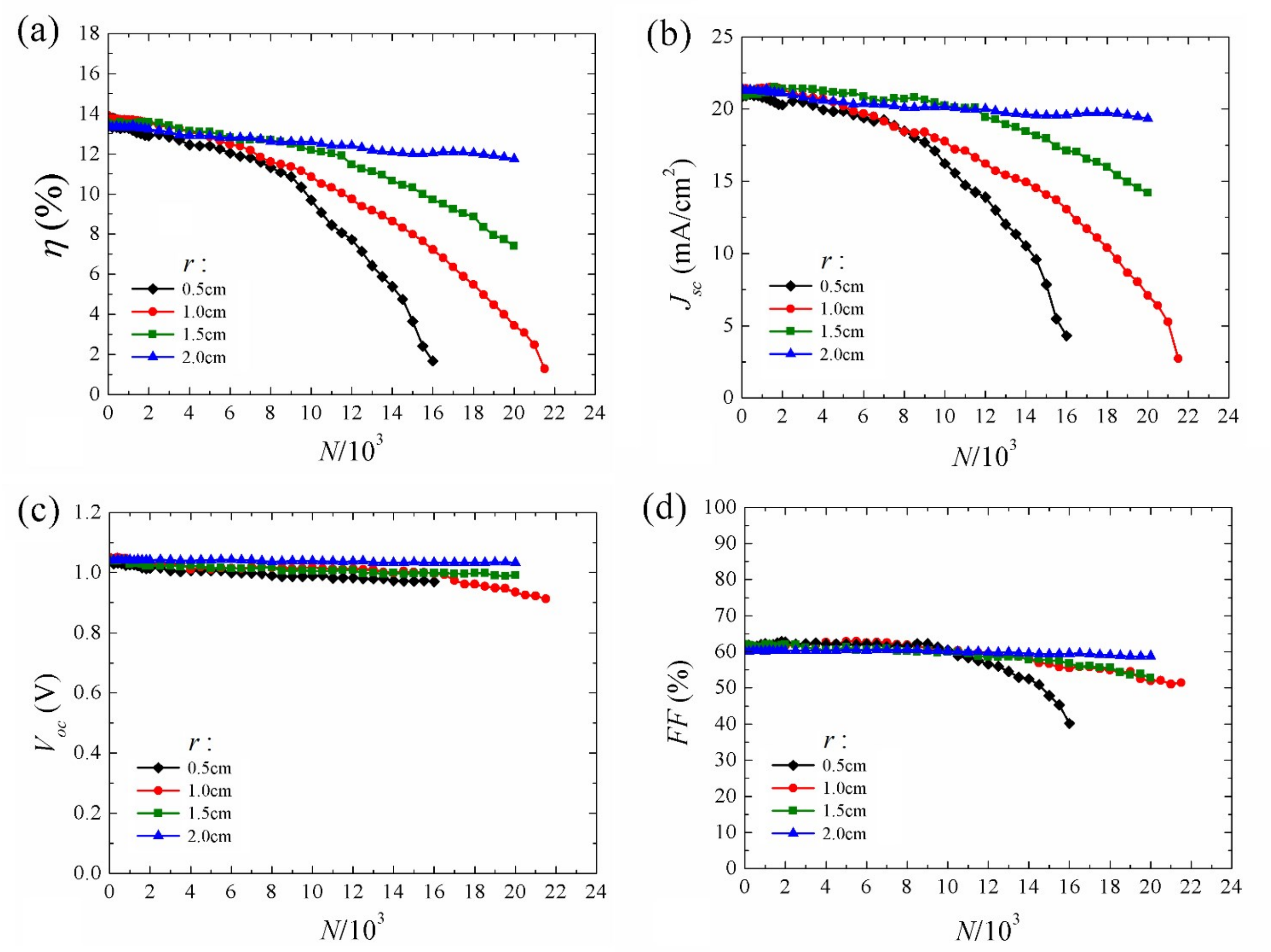

Figure S1 Effects of r and N on (a): η, (b): J_{sc}, (c): V_{oc} and (d): FF for the C1/E1/P1/H-FPSCs.

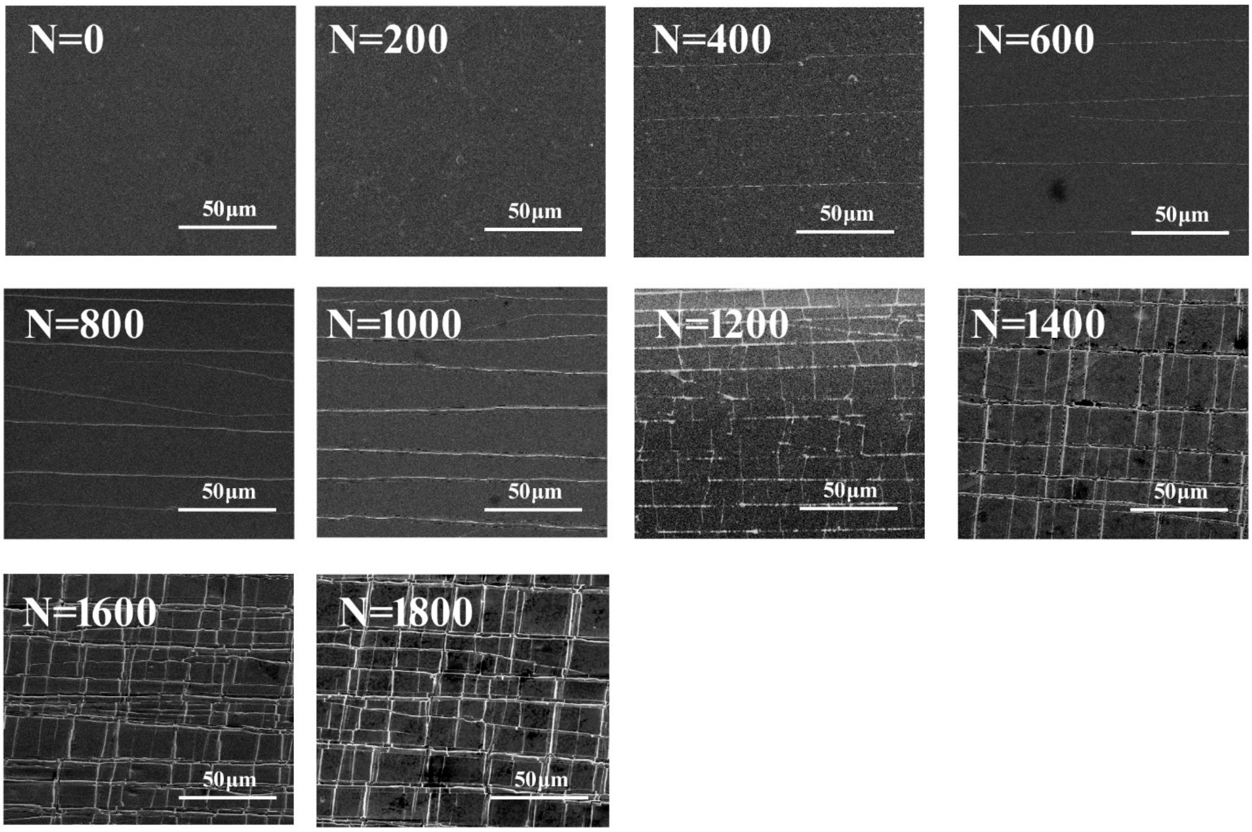

Figure S2 SEM images of bent ITO(185nm), when *r*=1.0cm.

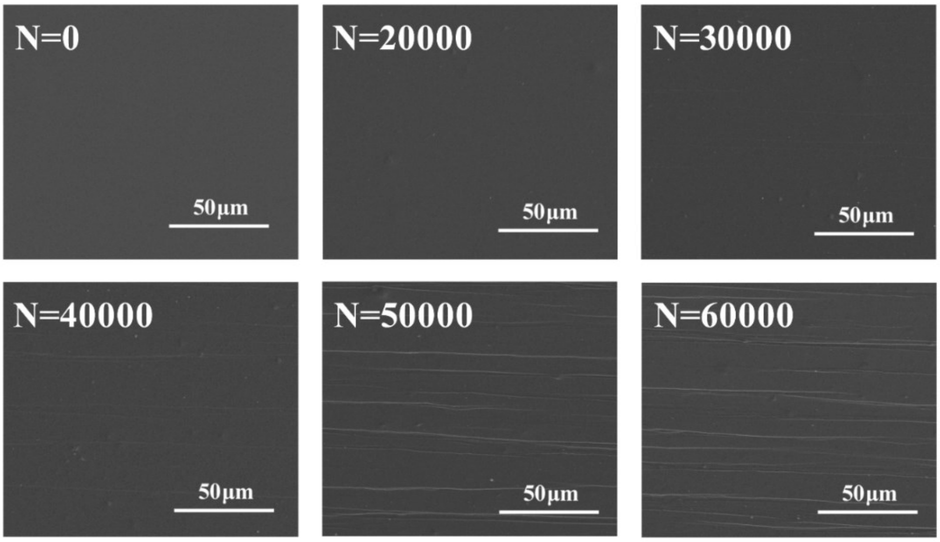

Figure S3 SEM images of bent PEDOT:PSS:Li, when *r*=1.0cm.

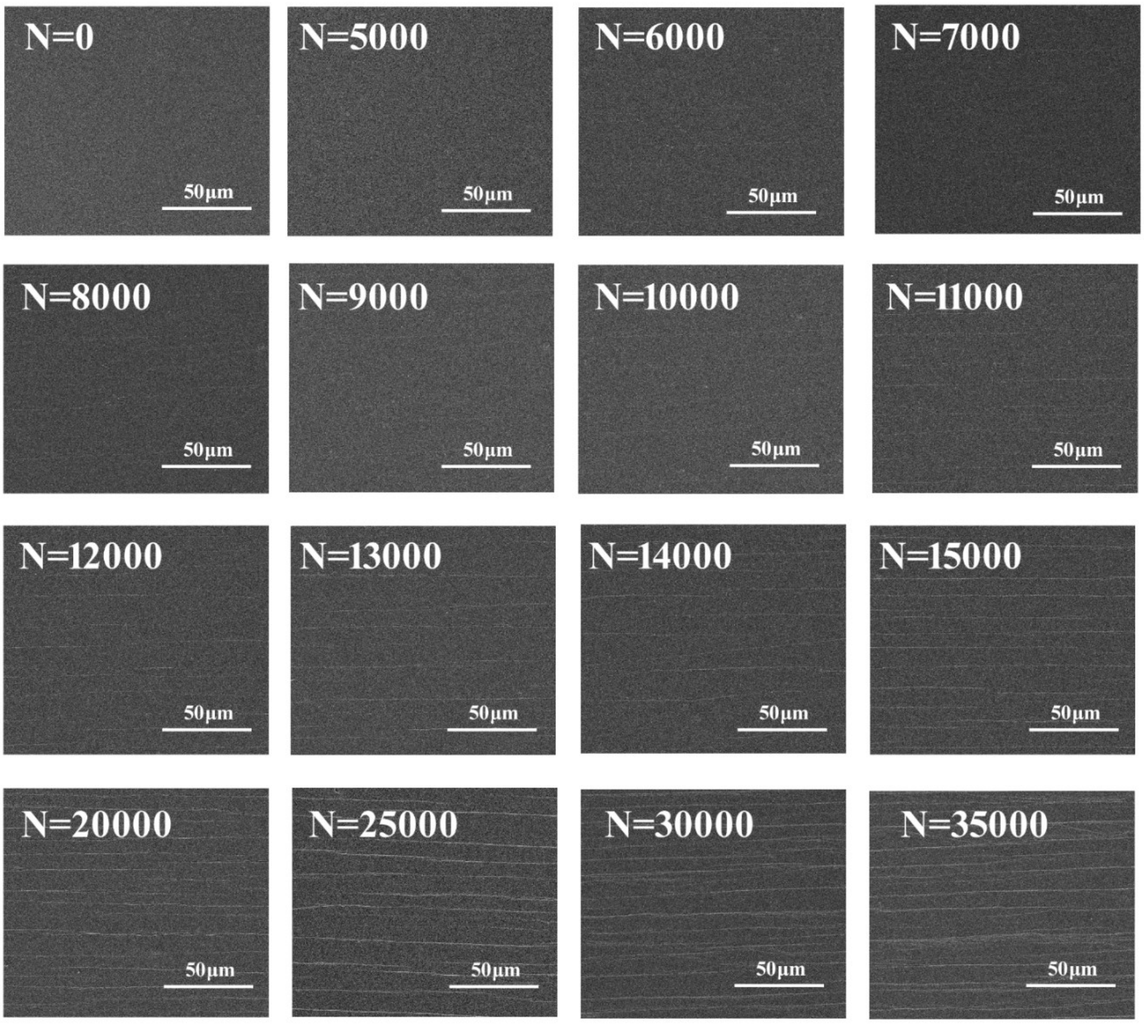

Figure S4 SEM images of bent PEDOT:PSS:Li/ITO(20nm), when *r*=1.0cm.

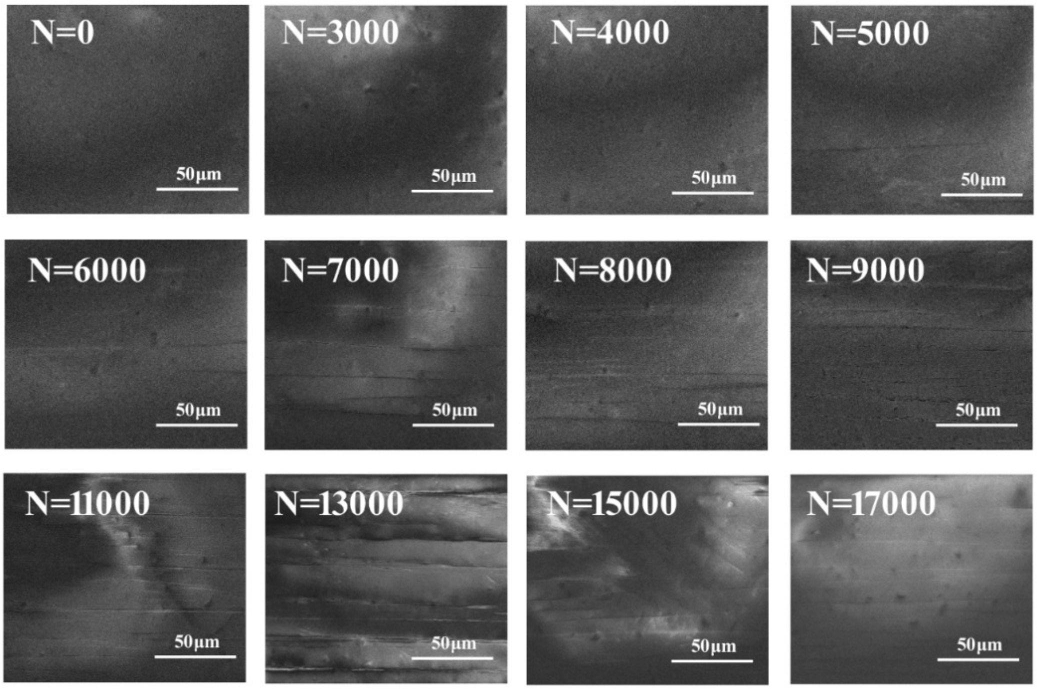

Figure S5 SEM images of bent SnO_2, when *r*=1.0cm.

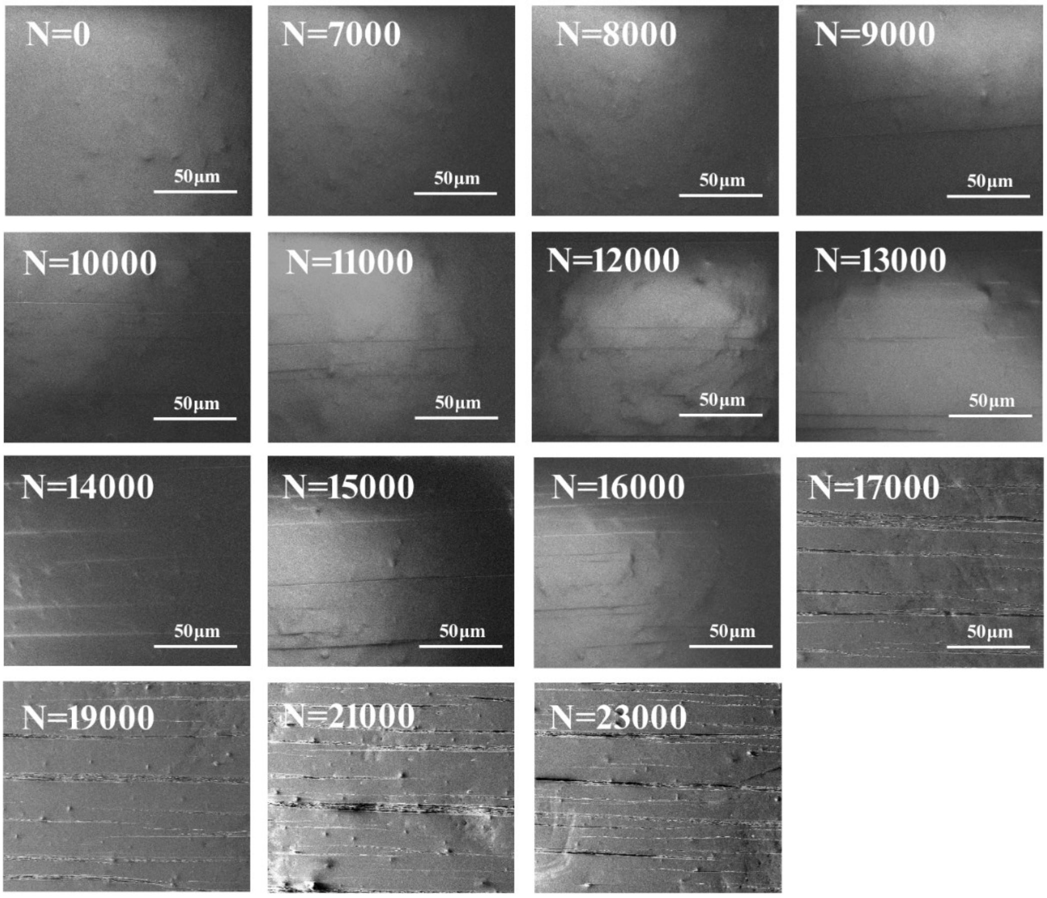

Figure S6 SEM images of bent SnO_2:Li, when *r*=1.0cm.

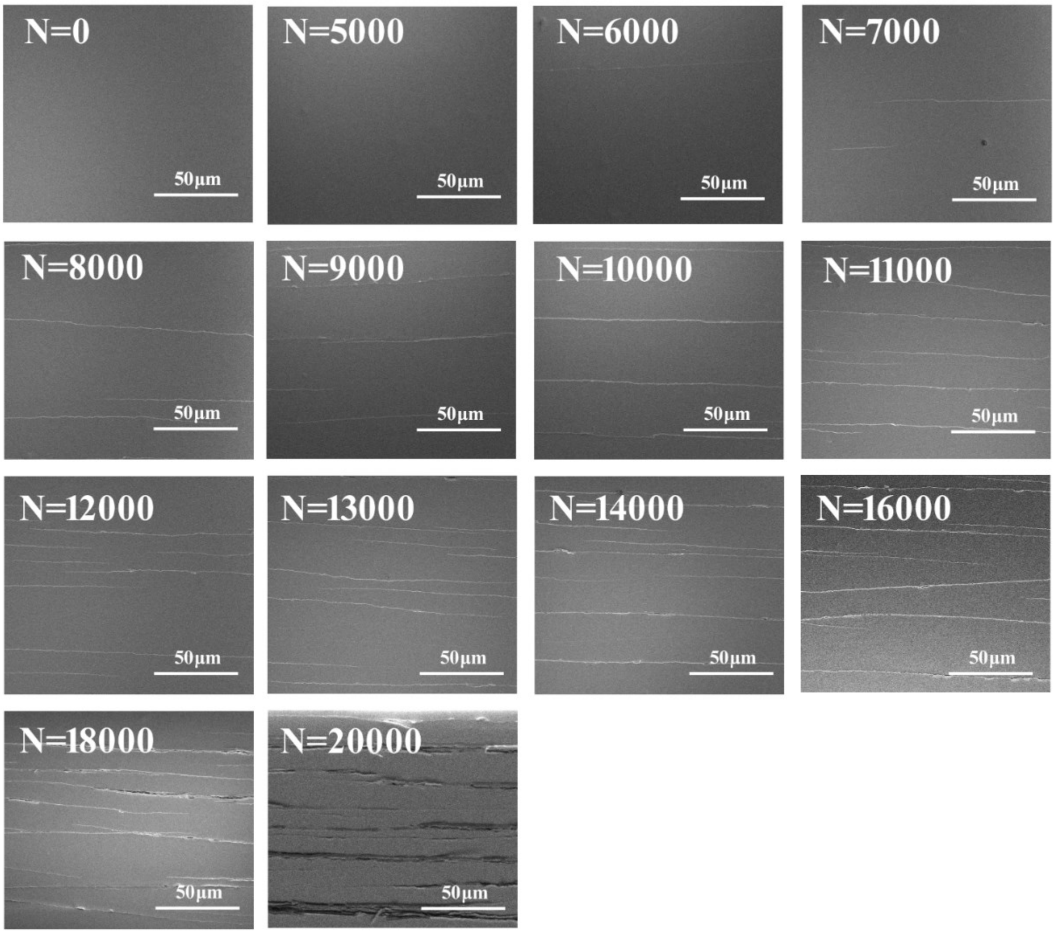

Figure S7 SEM images of bent $MAPbI_3$, when r=1.0cm.

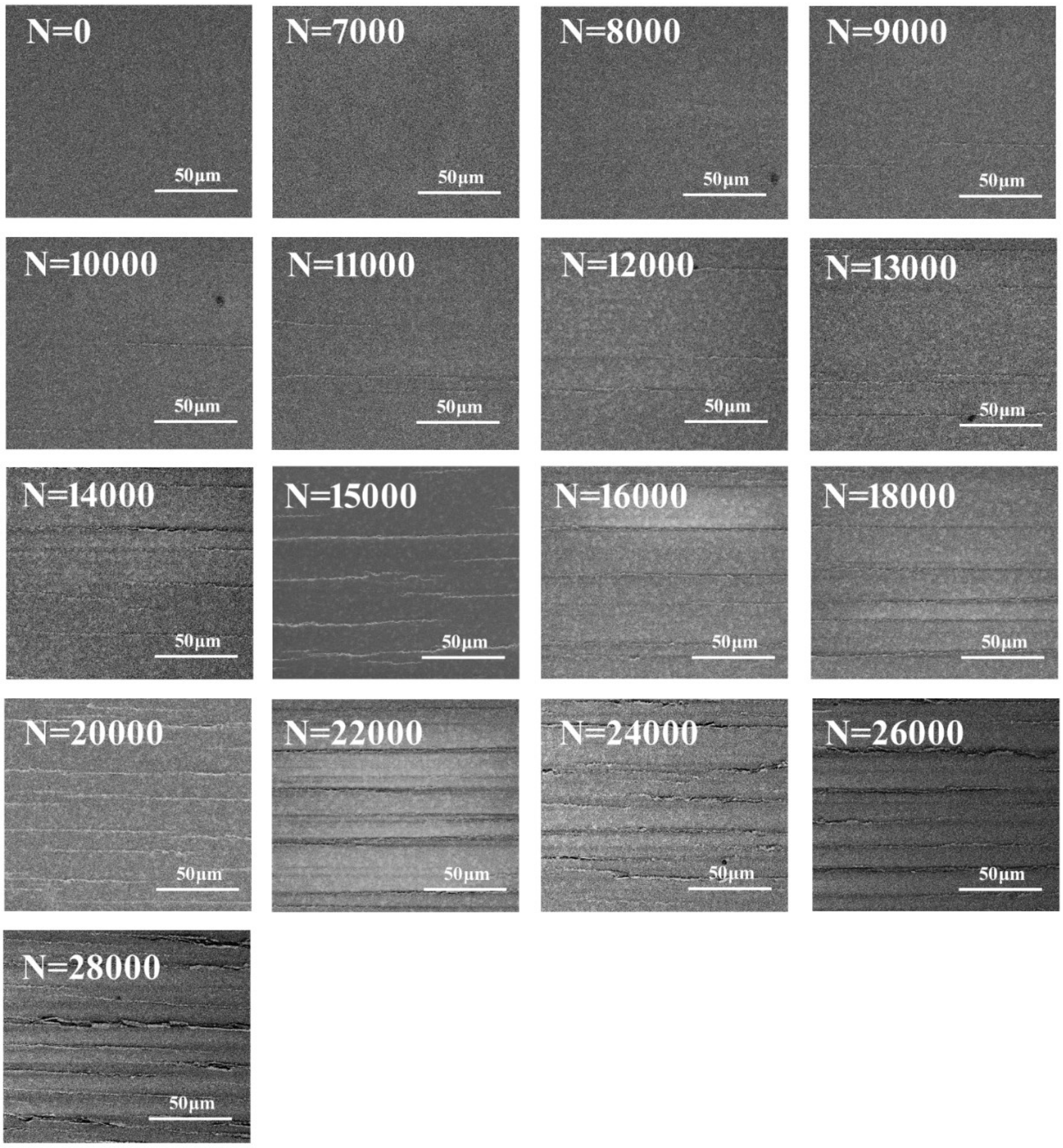

Figure S8 SEM images of bent $MAPbI_3$:PbI_2-MMI, when *r*=1.0cm.

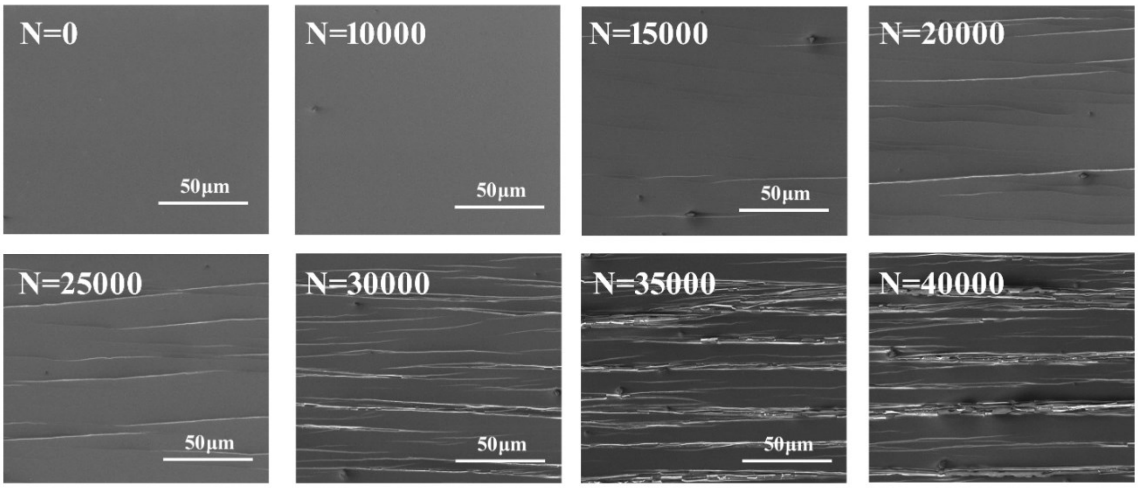

Figure S9 SEM images of bent spiro-OMeTAD, when *r*=1.0cm.

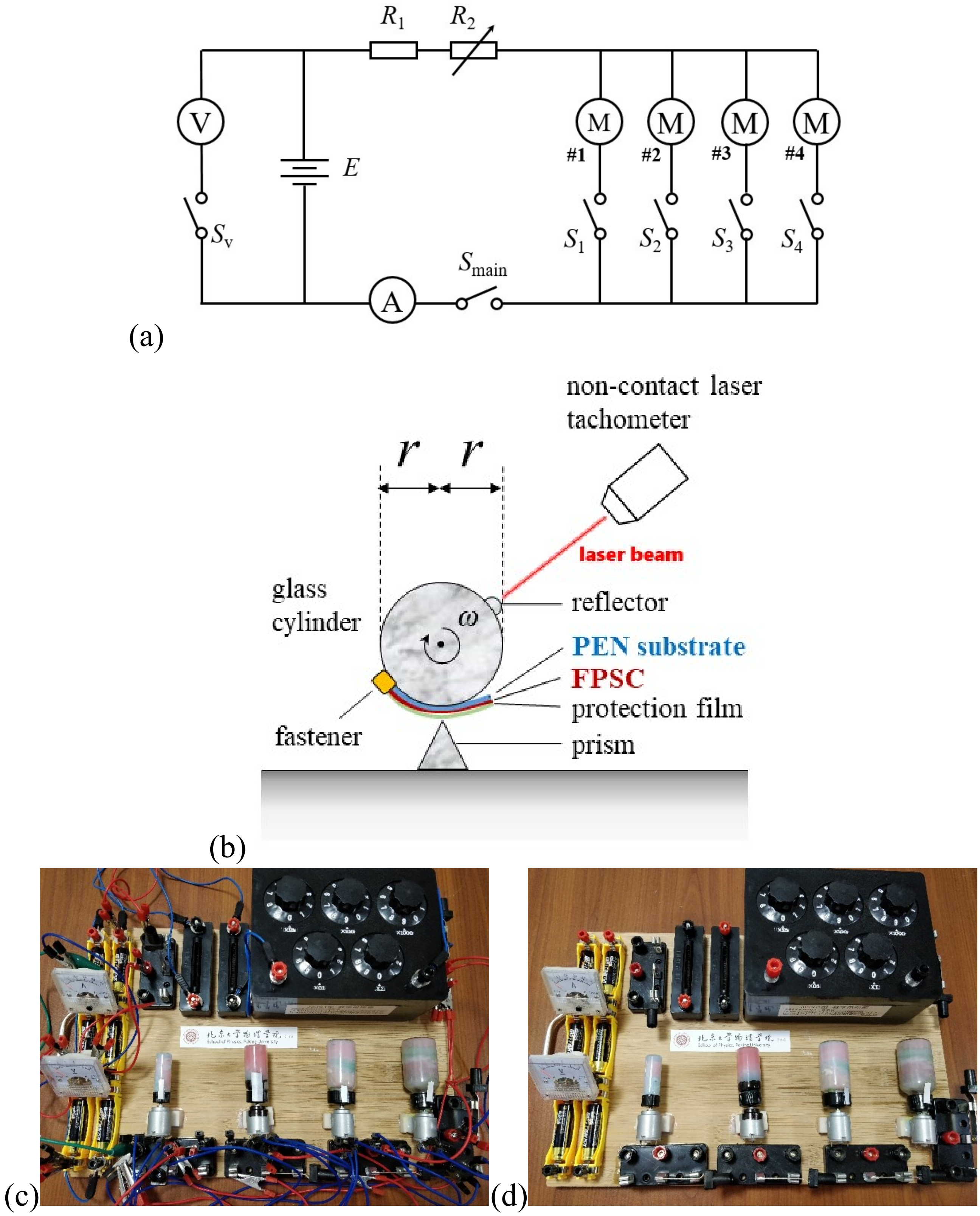

Figure S10 (a): Circuit diagram of the home-made bending machine; (b): illustration of the bending process; (c)~(d): photographs of the machine with and without connecting the circuit.

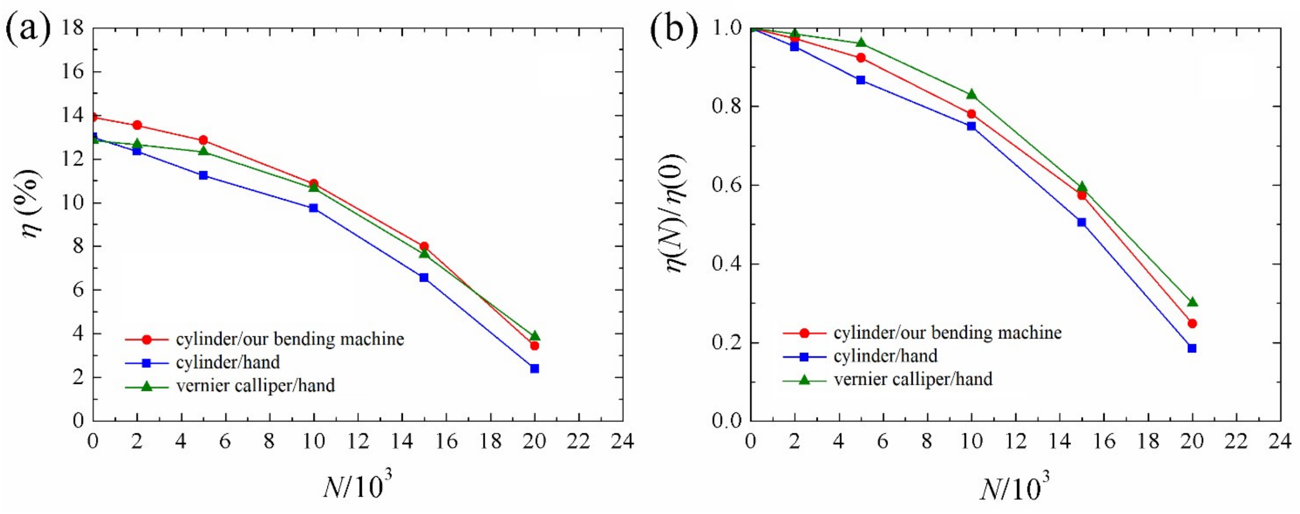

Figure S11 Effects of N on (a): $\eta(N)$, (b): $\eta(N)/\eta(0)$, for the C1/E1/P1/H-FPSCs. The FPSCs are bent by cylinder with our bending machine when r=1.0cm, by cylinder with hand when r=1.0cm, or by vernier caliper with hand at the average curvature radius of 1.0cm.

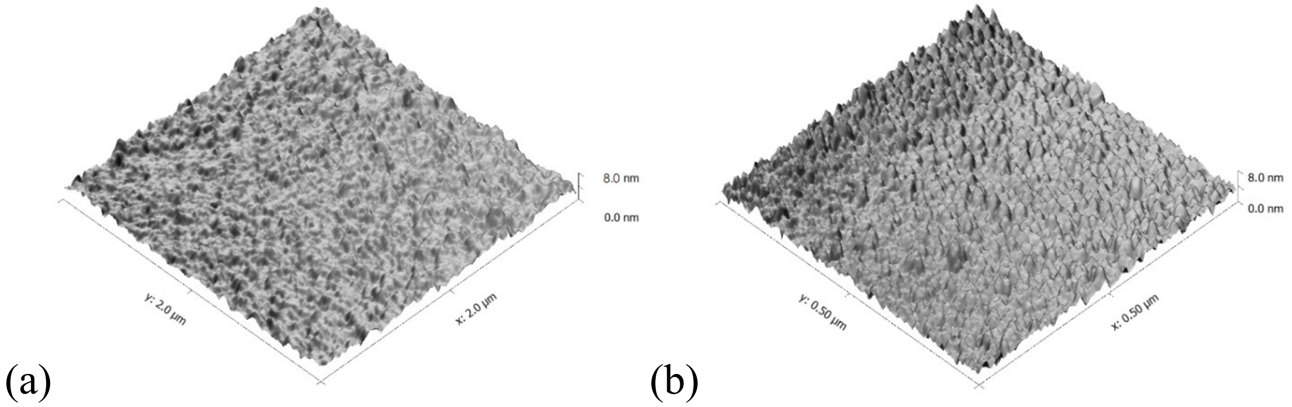

Figure S12 AFM images of unbent samples. (a): PEDOT:PSS:Li; (b): ITO(20nm).

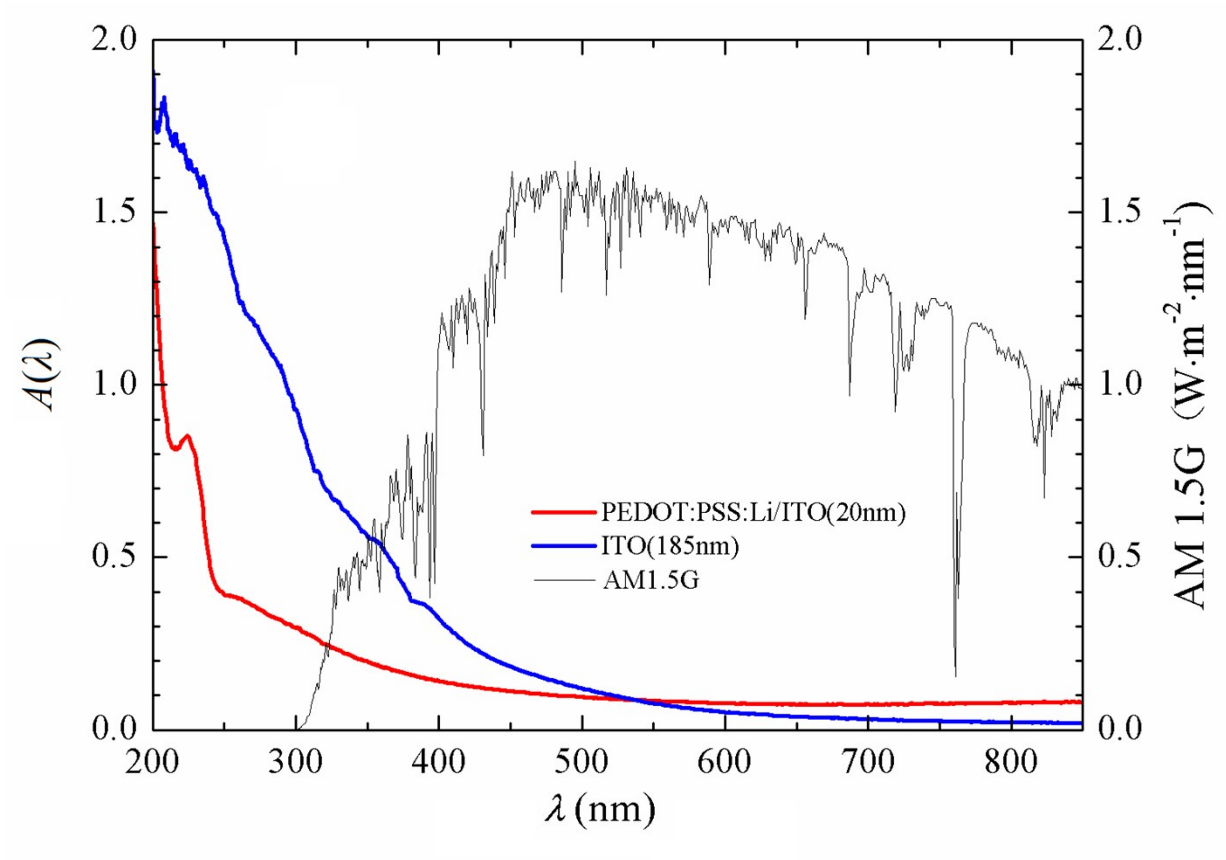

Figure S13 Absorbance spectra of unbent PEDOT:PSS:Li/ITO(20nm) and ITO(185nm), the AM 1.5G spectrum [1] is also showed.

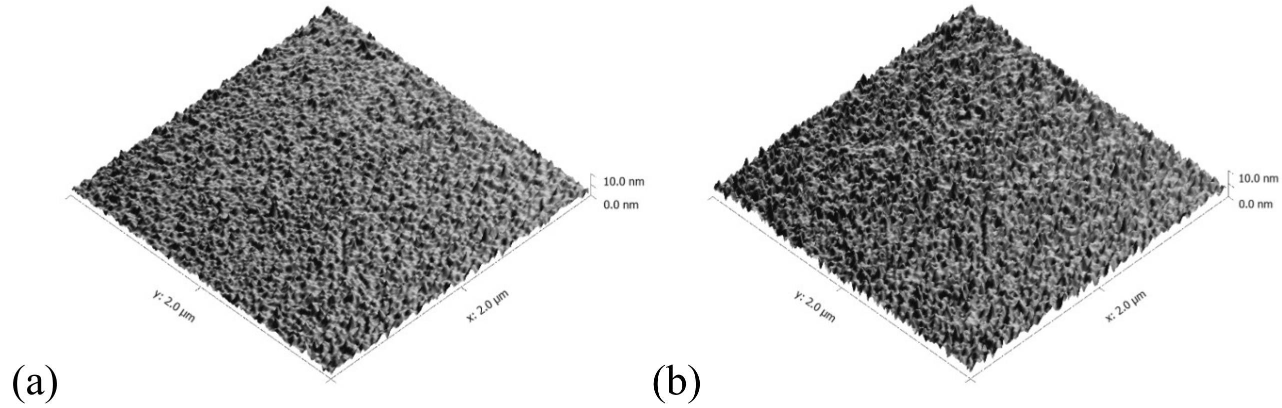

Figure S14 AFM images of the unbent electron transport layer samples. (a): SnO_2; (b): SnO_2:Li.

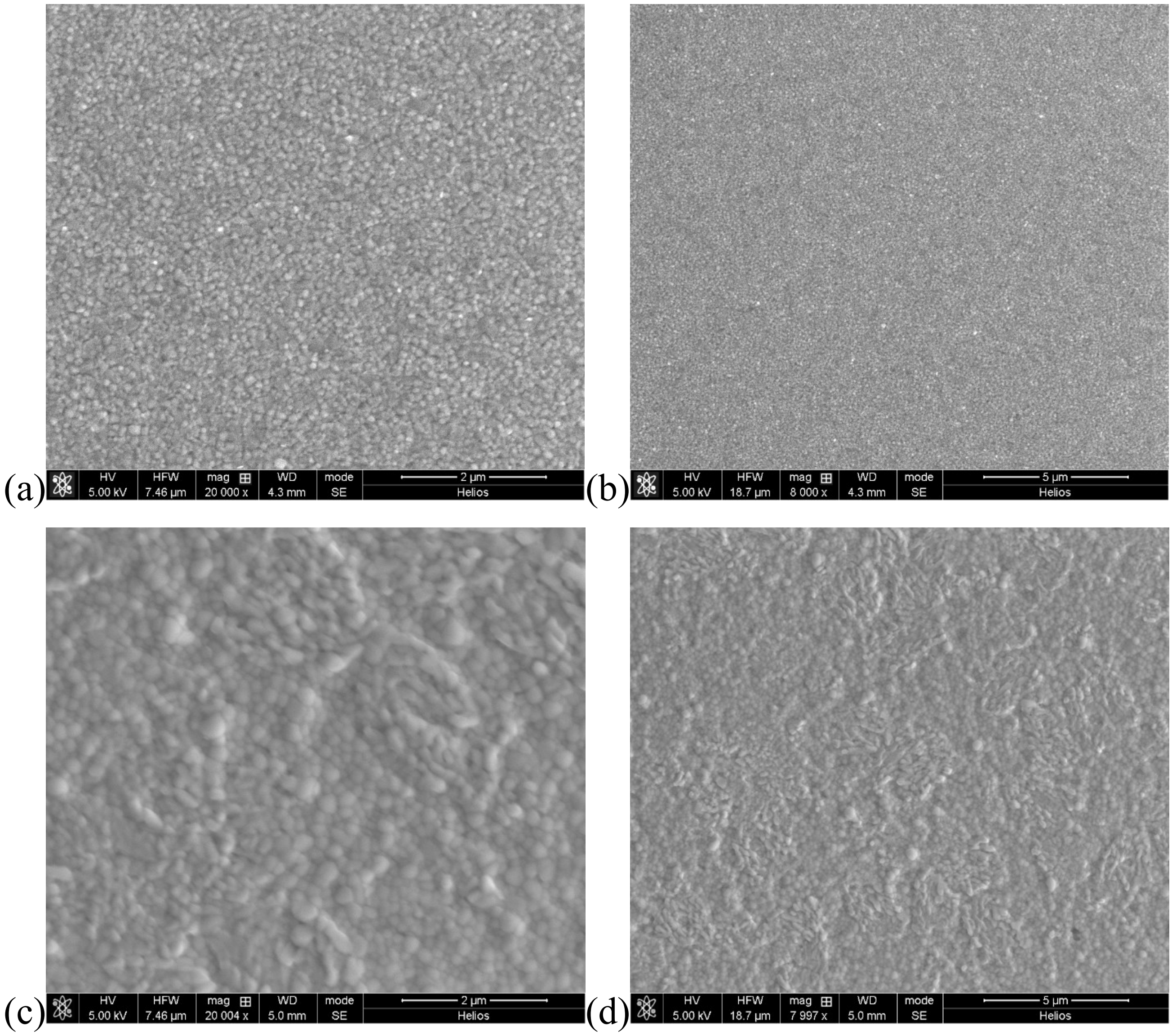

Figure S15 SEM images of unbent perovskite layer samples. (a)~(b): $MAPbI_3$; (c)~(d): $MAPbI_3$:PbI_2-MMI.

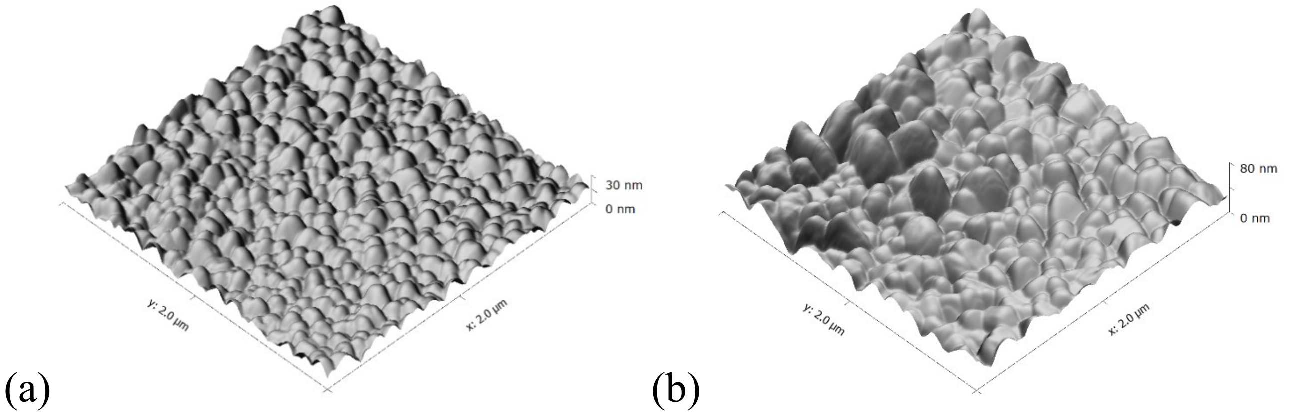

Figure S16 AFM images of unbent perovskite layer samples. (a): $MAPbI_3$; (b): $MAPbI_3$:PbI_2-MMI.

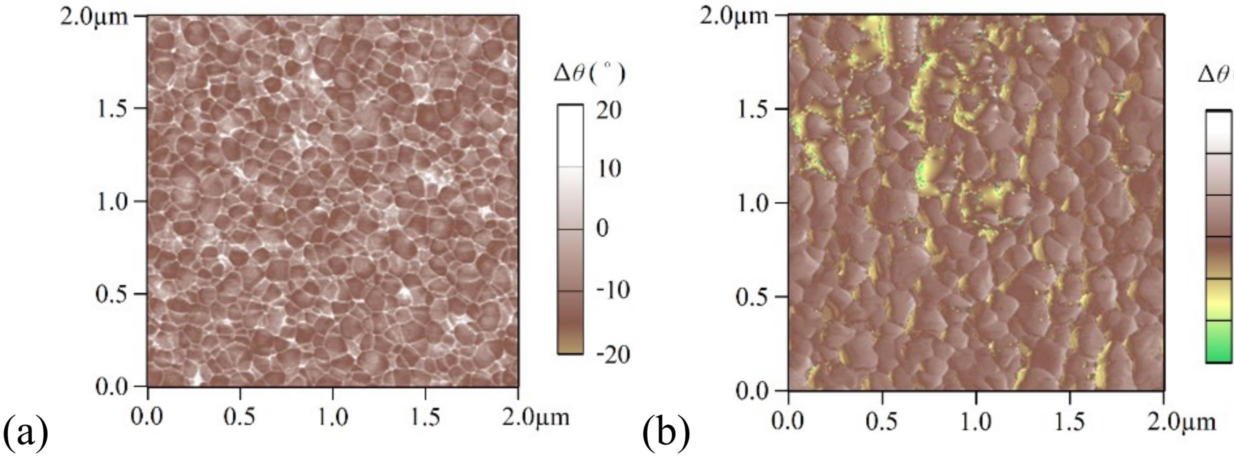

Figure S17: AFM phase images of unbent perovskite layer samples. (a) $MAPbI_3$; (b): $MAPbI_3$:PbI_2-MMI.

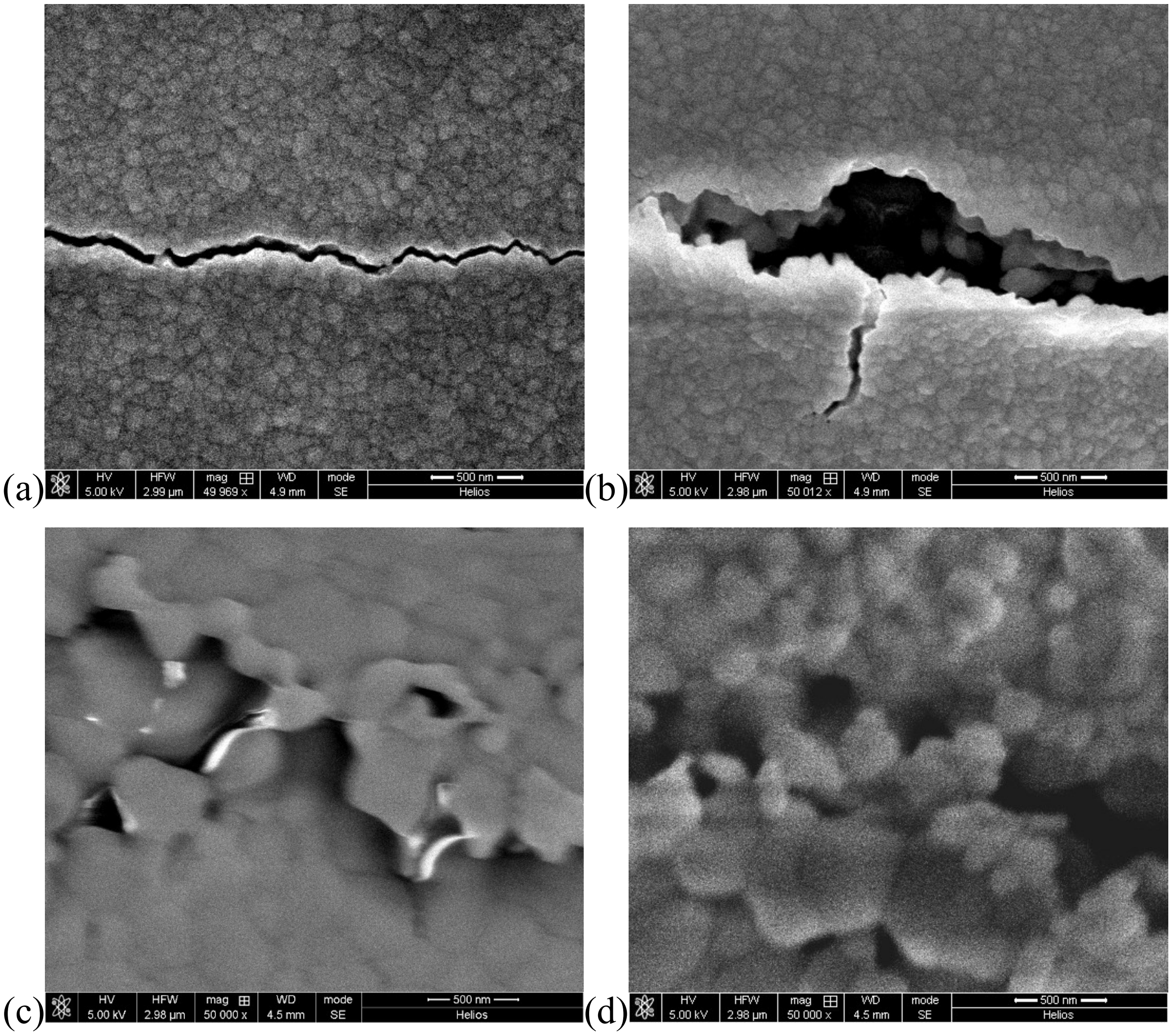

Figure S18 Close SEM observations of the cracks in the bent perovskite layer samples, when r=1.0cm. (a): $MAPbI_3$, N=8000; (b): $MAPbI_3$, N=16000; (c): $MAPbI_3$:PbI_2-MMI, N=12000; (d): $MAPbI_3$:PbI_2-MMI, N=20000.

Supplementary tables

Table S1. Non-universal abbreviations used in this article and their full names.

abbreviation	full name
ACN	acetonitrile
BW	backward
DTE	diethyl ether
ETL	electron transport layer
FIB	focused ion beam
FPSC	flexible perovskite solar cell
FW	forward
HTL	hole transport layer
IPA	iso-propanol
MMI	methimazole
PCE	power conversion efficiency
PEN	polyethylene naphthalate
UVCA	ultraviolet curing adhesive

Table S2 Results of N_f for the C0/E0/P0/H, C1/E0/P0/H, C1/E1/P0/H, C1/E0/P1/H, C1/E1/P1/H and C0/E1/P1/H architectured FPSCs, when r=1.0cm.

architecture η_f $N_f/10^3$	C0/E0 /P0/H	C1/E0 /P0/H	C1/E1 /P0/H	C1/E0 /P1/H	C1/E1 /P1/H	C0/E1 /P1/H
8%	0.81	7.10	11.23	9.41	14.98	0.87
5%	1.13	11.41	15.82	12.62	18.48	1.29
2%	1.36	14.58	19.14	15.36	21.27	1.59

Table S3 Results of improvement ratio for the C1/E0/P0/H, C1/E1/P0/H, C1/E0/P1/H, C1/E1/P1/H and C0/E1/P1/H architectured FPSCs, when r=1.0cm.

architecture η_f improvement ratio	C1/E0/P0/H	C1/E1/P0/H	C1/E0/P1/H	C1/E1/P1/H	C0/E1/P1/H
8%	8.74	13.83	11.58	18.44	1.07
5%	10.07	13.97	11.14	16.31	1.13
2%	10.72	14.07	11.29	15.63	1.17

Table S4 $\varphi_i(0)$ for the unbent constituent layers in our FPSCs obtained by high resistance method.

constituent layer	abbreviation	$\varphi_i(0)$ (S)
ITO(185nm)	C0	6.48×10^{-2}
PEDOT:PSS:Li/ITO(20nm)	C1	1.58×10^{-2}
SnO_2	E0	1.64×10^{-11}
SnO_2:Li	E1	2.31×10^{-11}
$MAPbI_3$	P0	5.83×10^{-13}
$MAPbI_3$:PbI_2-MMI	P1	6.89×10^{-13}
spiro-OMeTAD	H	2.31×10^{-11}

Table S5 Fitting results of m_{iV}, i=1, 2, 3 and 4, and the corresponding minimum χ_V^2, for the C0/E0/P0/H, C1/E0/P0/H, C1/E1/P0/H, C1/E0/P1/H, C1/E1/P1/H and C0/E1/P1/H architectured FPSCs.

architecture	C0/E0/P0/H	C1/E0/P0/H	C1/E1/P0/H	C1/E0/P1/H	C1/E1/P1/H	C0/E1/P1/H
$\chi_V^2/10^{-3}$	0.03	0.74	1.76	0.42	0.25	0.02
m_{1V}	0.0599	0.0018	0.0021	0.0041	0.0024	0.0789
m_{2V}	0.0356	0.1105	0.1610	0.0086	0.0016	0.1279
m_{3V}	0.0195	0.0015	0.0070	0.0057	0.0432	0.0140
m_{4V}	0.0008	0.0058	0.0014	0.0018	0.0015	0.0076

Table S6 Fitting results of m_{iF}, i=1, 2, 3 and 4, and the corresponding minimum χ_F^2, for the C0/E0/P0/H, C1/E0/P0/H, C1/E1/P0/H, C1/E0/P1/H, C1/E1/P1/H and C0/E1/P1/H architectured FPSCs.

architecture	C0/E0/P0/H	C1/E0/P0/H	C1/E1/P0/H	C1/E0/P1/H	C1/E1/P1/H	C0/E1/P1/H
$\chi_F^2/10^{-3}$	1.61	1.13	0.47	0.18	0.32	1.02
m_{1F}	0.3248	0.0025	0.0023	0.0017	0.0025	0.3015
m_{2F}	0.2667	0.2318	0.0812	0.1964	0.0636	0.0649
m_{3F}	0.0523	0.0536	0.0602	0.0488	0.0452	0.0419
m_{4F}	0.0081	0.0075	0.0060	0.0076	0.0083	0.0093

Table S7 Hall measurement results for unbent ITO(185nm) and PEDOT:PSS:Li.

sample	d (nm)	μ (cm^2·V^{-1}·s^{-1})	carrier concentration p or n (×10^{20}cm^{-3})	R_{sq} (Ω/□)
ITO(185nm)	185	84.20	2.65	15.13
PEDOT:PSS:Li	120	61.60	1.34	63.15

Table S8 AFM measurement results of <Φ> and s_z for unbent SnO_2 and SnO_2:Li.

sample	<Φ> (nm)	s_z (nm)
SnO_2	16	0.7
SnO_2:Li	21	1.1

Table S9 <Φ> obtained by SEM and AFM, and s_z (nm) obtained by AFM, for unbent $MAPbI_3$ and $MAPbI_3$:PbI_2-MMI.

sample	<Φ> (nm) obtained by SEM	<Φ> (nm) obtained by AFM	s_z (nm) obtained by AFM
$MAPbI_3$	151	137	4.1
$MAPbI_3$:PbI_2-MMI	319	308	6.3

1. Home-made bending machine

We designed a home-made bending machine driven by electricity to bend the flexible perovskite solar cells (FPSCs) automatically. The machine's circuit diagram, illustration of the bending process, photographs of the machine with and without connecting the circuit are presented in Figures S10(a)~(d), respectively. A 9V direct current power source is used to drive the rotation of the motors. R_1 is set to protect the circuit from large current, and there is: R_1=15Ω. By observing the amperemeter, it is guaranteed that the current flowing through the circuit is less than 2.0A. The motor's rotation axis coincides with that of the glass cylinder. The bending radius, r, equals the cylinder's radius. The FPSCs were bent with the bending radius of 0.5, 1.0, 1.5 or 2.0cm according to need. The reflector is fixed on the cylinder, and the digital non-contact laser tachometer records the rotation angular speed of the cylinder, ω. The timer records the elapsed time since the rotation starts, t. The bending cycle, N, is calculated by: $N=\omega t$. The decade resistance box, R_2, can be modified from 0.1Ω to 9999.9Ω with the minimum precision of 0.1Ω. With R_2, the current that drives the motor is controlled, so that ω can be modified according to need. In our experiment, ω was fixed as 120.0rpm.

In literature, to study the influences of bending on the power conversion efficiencies (PCEs) for FPSCs, their bending methods are summarized as: by cylinder with hand, in which r equals the cylinder's radius[2-4], or by vernier caliper with hand, in which the average curvature radius of the FPSC was calculated by geometry[5, 6]. The effects of N on $\eta(N)$ and $\eta(N)/\eta(0)$, for our C1/E1/P1/H-FPSCs, when they were bent by cylinder with our bending machine at the bending radius of 1.0cm, by cylinder with hand at the bending radius of 1.0cm, and by vernier caliper with hand at the average curvature radius of 1.0cm, are presented in Figures S11(a) and (b), respectively. When N increases, the $\eta(N)$ and $\eta(N)/\eta(0)$ for the FPSCs bent with the three different bending methods agree with each other. Of these three methods, it is advantageous to use our bending machine. Firstly, by using our bending machine, we are able to precisely control the parameters such as bending radius, bending speed, and etc. Secondly, in most researches the FPSCs were bent with hand, and the bending cycle, N, was very limited. It is very difficult to investigate the performance of the FPSC when N is quite large. With our bending machine driven by electricity, we performed bending experiment with even more than 20000 bending cycles. In daily use, it is very common for flexible devices to endure so many bending cycles.

2. Improvement of cathode

Wang et al. [7] used a one-step annealing process to fabricate the PEDOT:PSS:Li material, which exhibits both wonderful electrical conductivity and excellent anti-bending ability. In their research, after spin-coating on substrate, PEDOT:PSS:Li was annealed at 130℃ for 15 min. We managed to improve this method, and introduced a two-step annealing method to fabricate PEDOT:PSS:Li.

The annealing temperature of PEDOT:PSS:Li cannot be larger than the glass transition temperature, T_g, for the polyethylene naphthalate (PEN) substrate, or approximately 155℃. In our method, after spin-coating on PEN substrate, PEDOT:PSS:Li was first annealed to 100℃, i.e. the boiling point of H_2O, for 5min. Then it was annealed to 150℃ for 10min.

The atomic force microscope (AFM) images of PEDOT:PSS:Li fabricated by our two-step annealing method is presented in Figure S12(a). It is calculated that the surface roughness, s_z, of the PEDOT:PSS:Li fabricated by our two-step annealing method, is only 0.8nm. The Hall measurement results for unbent ITO(185nm) and PEDOT:PSS:Li are listed in Table S7. It can be seen that although PEDOT:PSS is an organic material, after doping it with LiTFSI and treating it with our two-step annealing method, the electrical properties of the resulting PEDOT:PSS:Li is close to those of the conventional inorganic ITO(185nm) material. For example, the sheet resistance, R_{sq}, for PEDOT:PSS:Li, achieved as small as 63.15Ω/□. The PEDOT:PSS:Li mentioned in the following discussions are all fabricated by our two-step annealing method.

The fabrication of the ITO(20nm) layer by magnetron sputtering on PEDOT:PSS:Li must not damage PEDOT:PSS:Li. Therefore, the sputtering power should be as low as possible. The direct current mode with the sputtering power of 10W was used. The sputtering process was performed in Ar atmosphere. The gas-flow of Ar was 25sccm. The air pressure of luminance build-up was 12mTorr. In sputtering, the air pressure in the chamber was fixed as 0.15μTorr. The sputtering speed was 1.33nm/min, and the sputtering time was 15min. The substrate was rotated at 20rpm during the sputtering process. With the laser infrared thermometer (Tecman TM600), in sputtering, the substrate temperature inside the chamber was measured as 19.40±0.93℃, which is only slightly larger than the room temperature, i.e. 18.50℃. Thus, the temperature rise during the magnetron sputtering process will not influence the PEDOT:PSS:Li layer. The AFM image of ITO(20nm) after annealing at 140℃

for 1h is presented in Figure S12(b). The ITO(20nm) layer surface is flat and uniform, and the ITO grains are observed. It is calculated that its average grain size, $<\Phi>$, is 17nm, and the s_z is only 0.8nm.

The absorbance spectra, $A(\lambda)$, of PEDOT:PSS:Li/ITO(20nm) and ITO(185nm) are compared in Figure S13. When λ is smaller than approximately 540nm, the $A(\lambda)$ of PEDOT:PSS:Li/ITO(20nm) is smaller than that of ITO(185nm), and vice versa. When λ is in the range of approximately 400~600nm, where the AM 1.5G irradiation is the largest [1], the $A(\lambda)$ of PEDOT:PSS:Li/ITO(20nm) is as small as approximately 0.1, which exhibits good transparency.

The scanning electron microscope (SEM) images of bent ITO(185nm), when r=1.0cm, are presented in Figure S2. Horizontal cracks start to appear when the bending cycle, N, is only 400. The number of the horizontal cracks increases as N increases thereafter. When N is 1200, vertical cracks start to appear. The anti-bending ability of ITO(185nm) is poor.

The SEM images of bent PEDOT:PSS:Li, when r=1.0cm, are presented in Figure S3. Only horizontal cracks are observed. When N equals 30000, the horizontal cracks start to appear. The SEM images of bent PEDOT:PSS:Li/ITO(20nm), when r=1.0cm, are presented in Figure S4. Only horizontal cracks are observed. When N equals 6000, the horizontal cracks start to appear. The anti-bending ability of PEDOT:PSS:Li/ITO(20nm) is satisfactory.

Therefore, PEDOT:PSS:Li/ITO(20nm) is used as the improved cathode in our FPSCs. It is marked as “C1” in the article.

3. Improvement of ETL

In the early stages of development for perovskite solar cells, when SnO_2 was used as the electron transport layer (ETL), the η was not satisfying, due to the large amount of recombination centers inside the SnO_2 layer[8].

A breakthrough was made by Jiang et al.’s research [8], in which high quality SnO_2 nanoparticle dispersion liquid was spin-coated on glass/ITO, and then the sample was annealed at 150°C to form the SnO_2 layer as the ETL. With this improvement, the η for their perovskite solar cell achieved as large as 19.9%[8]. After that, many researchers have tried to improve the SnO_2 layer as the ETL. Their methods include doping SnO_2 with Al [9], Ga [10], Y [11], Nb [12], and etc. Especially, Park et al. used lithium bis(trifluoromethylsulphonyl)imide (LiTFSI) to dope SnO_2, and the resulting SnO_2:Li layer was used as the ETL in the PEN/ITO/SnO_2:Li/methylammonium lead iodide ($MAPbI_3$)/2,2′,7,7′-tetrakis[*N*,*N*-

di(p-methoxyphenyl)amino]-9,9′-spirobifluorene (spiro-OMeTAD)/Au architectured FPSC [13]. The η for their FPSC achieved 14.78%, and it remained 95.8% and 91.9% of the initial value after 500 bending cycles, when the bending radius, r, equals 1.5cm and 1.0cm, respectively[13]. In their research, LiTFSI was mixed with $SnCl_2 \cdot H_2O$, and the mixture was dissolved in ethanol. The solution was spin-coated on PEN/ITO, and the sample was annealed at 185℃ for 3h to form the SnO_2:Li layer as the ETL. The dangling bongs within SnO_2 were passivated by the Li^+ ions, which led to a significant quality improvement of the ETL [13].

We combined the two methods proposed by Jiang et al. [8] and Park et al. [13] to fabricate the SnO_2:Li layer as the ETL for our FPSCs. In our method, 14.57mg of LiTFSI was mixed with 15.0g of the 3.0% (wt.%) SnO_2 nanoparticle dispersion liquid, so that in the resulting SnO_2:Li dispersion liquid, the molar ratio, n_{Sn}:n_{Li}, equals 100:1.7. The SnO_2:Li dispersion liquid was spin-coated on substrate at 3000rpm for 60s, and annealed at 150℃ for 30min to form the SnO_2:Li layer.

The AFM images of unbent SnO_2 and SnO_2:Li are presented in Figures S14(a) and (b), respectively. The SnO_2 and SnO_2:Li films are flat, uniform, and pinhole-free. The $<\Phi>$ and s_z results for SnO_2 and SnO_2:Li are compared in Table S8. The $<\Phi>$ and s_z of SnO_2:Li are larger than those of SnO_2.

The SEM images of bent SnO_2 and SnO_2:Li, when r=1.0cm, are presented in Figures S5 and S6, respectively. Au layer with thickness of 2nm was sputtered onto the samples to improve the surface electrical conductance and to obtain SEM images with better quality. In both SnO_2 and SnO_2:Li, after bending, only horizontal cracks are observed, and the number of the horizontal cracks increases as N increases thereafter. The cracks start to appear in SnO_2 and SnO_2:Li, when N is 5000 and 9000, respectively. The anti-bending ability of SnO_2:Li is better than that of SnO_2.

This phenomenon is explained as follows. Firstly, during the annealing process, when the sphere-shaped SnO_2 nanoparticles start to merge, many micro voids are formed among them. The voids are only partly occupied by the Sn^{4+} and O^{2-} ions, and they cannot be completely eliminated. We infer that in SnO_2, during bending, the cracks originated from these micro voids. In SnO_2:Li, the Li^+ ions fill in these voids among the SnO_2 nanoparticles, so that the micro voids are further eliminated. Secondly, we infer that the ionic bond strength of Li^+-O^{2-} is larger than that of Sn^{4+}-O^{2-}, which is deduced as follows. The melting point temperatures of Li_2O and SnO_2 are 1438℃ [14] and 1630℃ [15], respectively.

Their boiling point temperatures are approximately 2600°C [14] and 1800°C [15], respectively. Although the melting point temperature of Li_2O is slightly smaller than that of SnO_2, its boiling point temperature is much larger than that of SnO_2. Thirdly, we infer that by doping Li^+, a dispersion strengthening effect takes place in SnO_2:Li, so that the anti-bending ability largely increases.

Therefore, SnO_2:Li, in which the molar ratio, $n_{\mathrm{Sn}}:n_{\mathrm{Li}}$, equals 100:1.7, is used as the improved ETL in our FPSCs. It is marked as “SnO_2:Li”, or “E1” in the article.

4. Improvement of perovskite layer

To fabricate the FPSC with both wonderful power conversion efficiency and excellent anti-bending ability, the quality of the perovskite photovoltaic layer is critical. In a recent study by Liu et al.[16], the researchers used methimazole (MMI) to construct the surface “patch” by in situ converting residual PbI_2 at the $MAPbI_3$ grain boundaries [16]. An essential step in their method is dipping 50μL of the 2.0mg/mL MMI/iso-propanol (IPA) solution on $MAPbI_3$. After spin-coating and annealing, PbI_2–MMI complex was formed in the $MAPbI_3$ grain boundaries, and the quality of the once-treated perovskite layer was largely improved. Their optimized perovskite solar cell with the glass/ITO/SnO_2/$MAPbI_3$:PbI_2-MMI/spiro-OMeTAD/Ag architecture achieved the η as large as 20.10% [16].

We adopted the MMI-treating method and managed to improve it. In Liu et al.’s research, it is found that after $MAPbI_3$ was treated with the 2mg/mL MMI/IPA solution for only once, although the average grain size of the perovskite sample, $<\Phi>$, increased, the surface roughness, s_z, also largely increased, which could possibly lead to quality reduction of the perovskite layer. To reduce s_z, they tried many methods. For example, increasing the concentration of the MMI/IPA solution from 2.0mg/mL to 3.0mg/mL, or increasing the stay time of the MMI/IPA solution on $MAPbI_3$ surface, from 3s to 5s, or 7s. These approaches led to radical change of the morphology of the perovskite layer, so that $<\Phi>$ decreased, and s_z increased [16].

The improvement method proposed by us, is to further treat the once treated $MAPbI_3$:PbI_2–MMI with MMI solution again, but with different solvents, and less MMI concentration. The solvent used should dissolve the surface of the $MAPbI_3$ layer gently, rather than drastically changing the morphology. In our method, the $MAPbI_3$ precursor solution was prepared by mixing 461.0mg of PbI_2, 159.0mg of MAI, 78.0mg of dimethyl sulfoxide (DMSO) and 600.0mg of *N*,*N*-dimethylformamide (DMF). The 2.0mg/mL MMI/IPA and 0.5mg/mL MMI/(IPA/diethyl ether (DTE), v:v=1:4) solutions were also prepared. The $MAPbI_3$ precursor solution was spin-coated on the substrate at 1000rpm for 5s, and at 4000rpm for 60s. 10s after the spin-coating began, 0.8mL of DTE was dropped on the rotating sample as the second solvent. The sample was annealed at 90°C for 10min to form the pristine $MAPbI_3$ layer. 50μL of the 2.0mg/mL MMI/IPA solution was dipped on $MAPbI_3$. The sample was kept still for 3s, then it was spin-coated at 3000rpm for 30s, and annealed at 90°C for 10min to form the once treated $MAPbI_3$:PbI_2-MMI. 50μL of the 0.5mg/mL MMI/(IPA/DTE, v:v=1:4) solution was dipped on the once treated $MAPbI_3$:PbI_2-MMI. The sample was kept still for 3s, spin-coated at 3000rpm for 30s, and annealed at 90°C for 10min to form the twice treated $MAPbI_3$:PbI_2-MMI. In the following discussions, the $MAPbI_3$:PbI_2-MMI samples mentioned are all the twice treated $MAPbI_3$:PbI_2-MMI ones.

The SEM images of unbent $MAPbI_3$ and $MAPbI_3$:PbI_2-MMI are presented in Figures S15(a)~(b) and (c)~(d), respectively. The corresponding $<\Phi>$ of $MAPbI_3$:PbI_2-MMI is calculated as 319nm, which is larger than that of $MAPbI_3$, 151nm.

The AFM images of unbent $MAPbI_3$ and $MAPbI_3$:PbI_2-MMI are presented in Figures S16(a) and (b), respectively. The corresponding $<\Phi>$ and s_z results are listed in Table S9. The $<\Phi>$ obtained by SEM are also listed in Table S9, which agrees with the $<\Phi>$ obtained by AFM. The s_z of $MAPbI_3$:PbI_2-MMI, 6.3nm, is only slightly larger than that of $MAPbI_3$, 4.1nm. And, the $<\Phi>$ of $MAPbI_3$:PbI_2-MMI, 308nm, is much larger than that of $MAPbI_3$, 137nm.

The AFM phase images of unbent $MAPbI_3$ and $MAPbI_3$:PbI_2-MMI are presented in Figures S17(a) and (b), respectively. In $MAPbI_3$, PbI_2 mainly distributes in the grain boundaries of $MAPbI_3$, and its phase, $\Delta\theta$, is evidently larger than that of $MAPbI_3$. In $MAPbI_3$:PbI_2-MMI, PbI_2-MMI also mainly distributes in the grain boundaries of $MAPbI_3$, and its phase, $\Delta\theta$, is evidently smaller than that of $MAPbI_3$. PbI_2–MMI forms an inter-connected network in the grain boundaries of $MAPbI_3$. In Figure S17(b), we set $\Delta\theta<-5°$ as the judgement criteria to find PbI_2-MMI. The coverage ratios of PbI_2-MMI in Figure S17(b) is calculated as 10.97%.

The SEM images of bent $MAPbI_3$ and $MAPbI_3$:PbI_2-MMI, when r=1.0cm, are presented in Figures S7 and S8, respectively. For both of them, only horizontal cracks are observed, and the number of horizontal cracks increases as N increases thereafter. The cracks start to appear in $MAPbI_3$ and $MAPbI_3$:PbI_2-MMI when N is 6000 and 9000, respectively. The anti-bending ability of $MAPbI_3$:PbI_2-MMI is better than that of $MAPbI_3$.

Close SEM observations of a single crack in $MAPbI_3$ when N equals 8000 and 16000 are presented in Figures S18(a) and (b), respectively. The cracks in $MAPbI_3$ develop along the $MAPbI_3$ grain boundaries in zig-zag shape. The edges of the cracks are sharp and clear. When N increases, the width of the crack also increases.

Close SEM observations of a single crack in $MAPbI_3$:PbI_2-MMI when N equals 12000 and 20000 are presented in Figures S18(c) and (d), respectively. The cracks in $MAPbI_3$:PbI_2-MMI also develop along the $MAPbI_3$ grain boundaries. There are fiber-like PbI_2-MMI links that cling on the edges of the crack. During bending, the fiber-like PbI_2-MMI links the $MAPbI_3$ grains and resists crack formation, which lead to better anti-bending ability.

With these considerations, $MAPbI_3$:PbI_2-MMI is used as the improved perovskite layer in our FPSCs. It is marked as “P1” in the article.

5. Anti-bending abilities of hole transport layer

The SEM images of bent spiro-OMeTAD, when r=1.0cm, are presented in Figure S9. Only horizontal cracks are observed. When N is approximately 15000, the horizontal cracks start to appear. When N increases, the number of the horizontal cracks increases as N increases thereafter. As micromolecular organic material, the anti-bending ability of spiro-OMeTAD is satisfactory. It is marked as “H” in the article.

6. Supplementary equations

Equations (10) and (11) can be rewritten as Equations (S1) and (S2):

$$V_{oc}^{\text{fit}}\left(N,m_{1V},m_{2V},m_{3V},m_{4V}\right)=V_{oc}\left(0\right)\cdot\left[f_1\left(N\right)\right]^{m_{1V}}\cdot\left[f_2\left(N\right)\right]^{m_{2V}}\cdot\left[f_3\left(N\right)\right]^{m_{3V}}\cdot\left[f_4\left(N\right)\right]^{m_{4V}} \quad \text{(S1)}$$

$$FF^{\text{fit}}\left(N,m_{1F},m_{2F},m_{3F},m_{4F}\right)=FF\left(0\right)\cdot\left[f_1\left(N\right)\right]^{m_{1F}}\cdot\left[f_2\left(N\right)\right]^{m_{2F}}\cdot\left[f_3\left(N\right)\right]^{m_{3F}}\cdot\left[f_4\left(N\right)\right]^{m_{4F}} \quad \text{(S2)}$$

where $f_i(N)$, i=1, 2, 3, and 4, are calculated according to Equation (5) with the parameters of a_i and b_i listed in Table 3.

For an FPSC with a decided architecture of C0/E0/P0/H, C1/E0/P0/H, C1/E1/P0/H, C1/E0/P1/H, C1/E1/P1/H or C0/E1/P1/H, the mean squared errors of the fittings for $V_{oc}(N)$ and $FF(N)$, which are marked as χ_V^2 and χ_F^2, are defined as the following:

$$\chi_V^{\ 2}\left(m_{1V},m_{2V},m_{3V},m_{4V}\right)=\frac{1}{q}\sum_{j=1}^{q}\left(\frac{V_{oc}\left(N_j\right)-V_{oc}^{\text{fit}}\left(N_j,m_{1V},m_{2V},m_{3V},m_{4V}\right)}{V_{oc}\left(N_j\right)}\right)^2 \quad \text{(S3)}$$

$$\chi_F^{\ 2}\left(m_{1F},m_{2F},m_{3F},m_{4F}\right)=\frac{1}{q}\sum_{j=1}^{q}\left(\frac{FF\left(N_j\right)-FF^{\mathrm{fit}}\left(N_j,m_{1F},m_{2F},m_{3F},m_{4F}\right)}{FF\left(N_j\right)}\right)^2 \tag{S4}$$

where j is positive integer that labels the experiment data points, q is the total number of the experiment data points, $V_{oc}(N_j)$ and $FF(N_j)$ are experiment data of $V_{oc}(N)$ and $FF(N)$ for the FPSC when N=N_j.

Supplementary references

1. Air Mass 1.5 Global spectrum, American Society for Testing and Materials http://rredc.nrel.gov/solar/spectra/am1.5/.
2. X. Xu, Q. Chen, Z. Hong, H. Zhou, Z. Liu, W.-H. Chang, P. Sun, H. Chen, N. D. Marco, M. Wang and Y. Yang, *Nano Lett.*, 2015, **15**, 6514-6520.
3. J. Yoon, H. Sung, G. Lee, W. Cho, N. Ahn, H. S. Jung and M. Choi, *Energy Environ. Sci.*, 2017, **10**, 337-345.
4. C. Roldán-Carmona, O. Malinkiewicz, A. Soriano, G. Mínguez Espallargas, A. Garcia, P. Reinecke, T. Kroyer, M. I. Dar, M. K. Nazeeruddin and H. J. Bolink, *Energy Environ. Sci.*, 2014, **7**, 994-997.
5. Y. Li, L. Meng, Y. Yang, G. Xu, Z. Hong, Q. Chen, J. You, G. Li, Y. Yang and Y. Li, *Nat. Commun.*, 2016, **7**, 10214.
6. J. Feng, X. Zhu, Z. Yang, X. Zhang, J. Niu, Z. Wang, S. Zuo, S. Priya, S. Liu and D. Yang, *Adv. Mater.*, 2018, **30**, 1801418.
7. Y. Wang, C. Zhu, R. Pfattner, H. Yan, L. Jin, S. Chen, F. Molina-Lopez, F. Lissel, J. Liu, N. I. Rabiah, Z. Chen, J. W. Chung, C. Linder, M. F. Toney, B. Murmann and Z. Bao, *Sci. Adv.*, 2017, **3**, e1602076.
8. Q. Jiang, X. Zhang and J. You, *Small*, 2018, **14**, 1801154.
9. H. Chen, D. Liu, Y. Wang, C. Wang, T. Zhang, P. Zhang, H. Sarvari, Z. Chen and S. Li, *Nanoscale Res. Lett.*, 2017, **12**, 238.
10. B. Roose, C. M. Johansen, K. Dupraz, T. Jaouen, P. Aebi, U. Steiner and A. Abate, *J Mater. Chem. A*, 2018, **6**, 1850-1857.
11. G. Yang, H. Lei, H. Tao, X. Zheng, J. Ma, Q. Liu, W. Ke, Z. Chen, L. Xiong, P. Qin, Z. Chen,

M. Qin, X. Lu, Y. Yan and G. Fang, *Small*, 2016, **13**, 1601769.

12. X. Ren, D. Yang, Z. Yang, J. Feng, X. Zhu, J. Niu, Y. Liu, W. Zhao and S. F. Liu, *ACS Appl. Mater. Interfaces*, 2017, **9**, 2421-2429.
13. M. Park, J.-Y. Kim, H. J. Son, C.-H. Lee, S. S. Jang and M. J. Ko, *Nano Energy*, 2016, **26**, 208-215.
14. Lithium Oxide, https://en.wikipedia.org/wiki/Lithium_oxide.
15. Tin(IV) Oxide, https://en.wikipedia.org/wiki/Tin(IV)_Oxide.
16. L. Liu, S. Huang, Y. Lu, P. Liu, Y. Zhao, C. Shi, S. Zhang, J. Wu, H. Zhong, M. Sui, H. Zhou, H. Jin, Y. Li and Q. Chen, *Adv. Mater.*, 2018, **30**, 1800544.